Solid State Ionics 320 (2018) 339–346

Contents lists available at ScienceDirect

Solid State Ionics

journal homepage: www.elsevier.com/locate/ssi

$LiMn_{1.8}Ni_{0.2}O_4$ nanorods obtained from a novel route using α-MnOOH precursor as cathode material for lithium-ion batteries

F.A. Vásquez[a], J.E. Thomas[b], A. Visintin[b], J.A. Calderón[a,*]

[a] Centro de Investigación, Innovación y Desarrollo de Materiales – CIDEMAT, Universidad de Antioquia UdeA, Calle70 N° 52 – 21, Medellín, Colombia
[b] Instituto de Investigaciones Fisicoquímicas Teóricas y Aplicadas (INIFTA), Facultad de Ciencias Exactas, Universidad Nacional de La Plata (UNLP), CCT La Plata-CONICET, CC 16, Suc. 4, 1900 La Plata, Argentina

ARTICLE INFO

Keywords:
Nanorod
LNM spinel
Lithium-ion battery
High-voltage cathode

ABSTRACT

Nanorod structures of $LiMn_{1.8}Ni_{0.2}O_4$ applicable as active cathode material for Li-ion batteries were synthesized from α-MnOOH and α-MnO_2 initial phases. The $LiMn_{1.8}Ni_{0.2}O_4$ spinel nanorods obtained from α-MnOOH using a novel, eco-friendly method showed higher purity than the traditional spinel obtained from α-MnO2. The showed charge capacity that was in the order of 122 mA h g^{-1} higher than similar active material reported in the literature, and it was able to keep > 80% of initial capacity at a charge rate of 5 C.

1. Introduction

The storage and production of energy are very important topics of discussion at the present time. To meet the energy demands of the growing world population, we must double our current energy production rate of 14 TW by 2050. This amounts to 130,000 TW h. This increase will be achieved without increasing CO_2 emissions, which has led to great interest in the production and storage of renewable energy [1,2]. For the transformation of a fossil fuel economy to one based on renewable technologies, we need to significantly improve our energy storage capacity. Taking into account the increase in energy dependence and per capita consumption in recent years, significant reductions in energy use in the short term will be very challenging to achieve. It is imperative to find new materials for the construction of sustainable batteries. Having identified desirable electrode materials, new methods are required for battery manufacture, with sustainability considered for each method. Currently, the automobile industry is implementing technologies free of greenhouse gas and with low environmental impact. In this field, electric vehicles (EVs) and hybrid vehicles (PHEVs) are the most suitable options to reduce the pollution generated by fossil fuels [3]. However, this technology has some drawbacks related to battery autonomy, stability and charge rate which need to be solved [4]. The lithium ion-battery presents characteristics that make it a promising technology, but more research is needed to improve its charge capacity and charge rate [5]. The charge rate and charge capacity are directly related to the structure, morphology and particle size of the active materials [6]. Manganese spinel structure has a high capacity and also has a 3D interstitial network which makes the lithium intercalation process easier within 8a sites [7]. This makes this material a good option for the development of cathodes for lithium-ion batteries with the necessary characteristics for use in appliances which present a high charge rate, and would therefore give more autonomy to electric cars. Several works concerning cathode materials with nanorod morphology and other kinds of nano-architecture have been published in recent years, with a view to finding new ways to improve lithium intercalation and stress dissipation during the charge-discharge process [6,8]. Also, different synthesis processes have been studied with the aim of increasing charge and rate capacity by obtaining nanorod structures with a short diffusion distance and high purity [9]. Studies have also focused on the addition of transition elements to the active material to increase the cathode potential and improve structural stability, with intermediates such as manganese oxide (α-MnO_2) [10] and manganese oxyhydroxide (α-MnOOH) having been obtained [11].

Several synthesis routes have been implemented to obtain spinel nanorods using different precursors with sulfate and potassium ions. In these cases the washing processes were difficult and impurities were found [9,12,13]. These drawbacks limit the performance of the cathode. Several techniques have been used to synthesize nanostructured $LiMn_2O_4$ cathodes, such as hydrothermal synthesis of α-MnO_2 [13] and α-MnOOH [9,14] by $KMnO_4$ precursor. Meanwhile, in other works α-MOOH was synthesized by $KMnO_4$ and $MnSO_4$ precursors, and it was necessary remove the sulfate and potassium ions during the washing process [12]. Although $KMnO_4$ allowed nanorod structures to be obtained, this process required other highly contaminant chemical compounds. Additionally, some impurities were found and the charge capacity was low [15].

* Corresponding author.
E-mail address: andres.calderon@udea.edu.co (J.A. Calderón).

https://doi.org/10.1016/j.ssi.2018.03.013
Received 14 February 2018; Accepted 9 March 2018

In this paper, an alternative route to obtain the α-MnOOH intermediate phase, with a view to in turn obtaining nanostructured manganese spinel such as LMNO, is presented. During the synthesis, the reaction sub-products are burned during a high temperature process (solid state stage synthesis). This alternative route diminishes the number of washing cycles and keeps the purity of the final product high. Additionally, the α-MnOOH nanorods obtained exhibit homogeneous diameter that is smaller than rods obtained in the literature [9,12], and enhance the cathode performance.

2. Experimental

2.1. Material synthesis

All reagents for synthesis were analytical and battery grade from Sigma Aldrich. In the first stage of the synthesis of the active cathode materials α-MnOOH and α-MnO_2 (for comparative purpose), nanorods were synthesized by hydrothermal methods according to the following procedures:

Synthesis of α-MnOOH: 0.04 mol of manganese acetate was dissolved in 100 ml of distilled water and 6.24 ml of NH_4OH (25%) was added. Then, 12 ml of H_2O_2 was added, while maintaining vigorous agitation. The solution was transferred into a Teflon-steel autoclave and heated at 140 °C for 15 h. After cooling to room temperature, the precipitate was washed with water and ethanol six times. Finally, the product was dried at 60 °C.

Synthesis of α-MnO_2: 0.08 mol of HCl (37%) was dissolved in 100 ml of distilled water and 0.02 mol of $KMnO_4$ was added while stirring. The solution was then transferred to a Teflon and steel autoclave and heated at 140 °C for 15 h. After cooling to room temperature the precipitate was washed with water and ethanol eight times. Finally, the precipitate was dried at 60 °C [13].

Once the α-MnOOH and α-MnO_2 phase materials were obtained, the process continued to the next stage for lithium and nickel incorporation. In this stage, stoichiometric mixtures of α-MnOOH and α-MnO_2 phases with lithium acetate and nickel acetate with a molar ratio of: 1.8:1.05:0.2 mol were prepared in ethanol-water solution. Then, NH_4OH was added to the solution until a pH 8.8 was reached in order to precipitate the nickel oxide on the nanorods surface. The solution was stirred at 80 °C to obtain a slurry, which was oven-dried at 60 °C. Finally, the mixture was annealed at 300 °C for 10 h in order to burn all the organic components, followed by heat treatment at 650 °C for 10 h in air atmosphere, which facilitates the lithium and nickel insertion during the formation of spinel structure.

2.2. Material characterization

Materials phase identification was carried out by Raman spectroscopy, X-ray diffraction (XRD), scanning electron microscopy (SEM) and transmission electron microscopy (TEM). Raman spectra were taken in a Horiba Jobin Yvon (Labram HR) Nikon (BX41) microscope, using a laser wave length of 632 nm, 0.6 D filter and 50× objective. The X-ray diffraction patterns (XRD) were performed using PANalytical reference equipment, with a 2θ scan between 10 and 80°. The flush angle between the specimen holder and the detector was fit at 5°. The XRD spectrum was analyzed by High Score Plus Software. Particle morphology and particle size were analyzed using SEM and TEM microscopes. The scanning electron microscopy (SEM) was carried out using JEOL JSM2490 CV equipment and the transmission electron microscopy (TEM) using Tecnai F20 Super Twin TMP equipment, with a field emission source and GATAN US 1000XP-P camera. HRTEM images were analyzed using Digital Micrograph software. The chemical composition was determined by Energy-dispersive X-ray spectroscopy (EDS).

Thermal analysis (TGA) was carried out on mixtures of nanorods, lithium acetate and nickel acetate. TGA curves were performed using TA instruments model Q500 equipment, under air atmosphere. The heating rate was 10 °C min^{-1} and the scan range was 25–900 °C.

2.3. Electrochemical characterization

All electrochemical tests were carried out in three-electrode cells (T-cells), with lithium foil metal as counter and reference electrodes. The working electrodes were prepared by coating aluminum foil with a slurry of 80 wt% active material, 10 wt% carbon black super P® and 10 wt% vinylidene fluoride in *N*-methyl pyrrolidone as solvent, and drying this in a vacuum oven at 80 °C for 4 h. The electrolyte used was 1.5 mol $LiPF_6$, in ethylene carbonate (EC) and dimethyl carbonate (DMC) with a volume ratio of (1:2) solution. All the cells were assembled under Argon atmosphere in a MBraun glove-box working under 1 ppm of oxygen and moisture.

The first 25 cycles were then performed at 0.5 C. After that, impedance spectroscopy, cyclic voltammetry and rate capability were carried out. Finally, the samples were cycled at 1 C for a further 100 cycles. The impedance spectroscopy was measured at open circuit voltage (OCV) for different states of charge (SOC), specifically 0, 50 and 100% of SOC, in a frequency range from 20 kHz to 1 mHz with an AC oscillation of 10 mV. In the third step, cyclic voltammetry was conducted at scan rates of 0.1, 0.2, 0.5 and 1 mV s^{-1} between 3 and 5.2 V. Finally, the rate capability was repeated twice at 0.1, 0.2, 0.5, 1, 2, 5, and 10 C for all samples. The electrochemical tests were done using a MSTAT4 multichannel battery tester from Arbin and a Pgstat302N potentiostat from Metrohm Autolab.

3. Results and discussion

3.1. Characterization of nanorods structure precursors

SEM images and Raman spectra of α-MnO_2 and α-MnOOH phase materials prepared in the first stage of the synthesis are shown in Fig. 1. The Raman spectra of the α-MnO_2 and α-MnOOH nanorod materials are shown in Fig. 1a and c respectively. This technique makes it possible to clearly differentiate both manganese oxide and manganese oxyhydroxide phases. The Raman spectrum in Fig. 1a shows vibration bands at 180, 379, 502, 573 and 630 cm^{-1}, characteristic of α-MnO_2. The main band of the α-MnO_2 at 573 cm^{-1} is attributed to the Mn−O vibration [13,16]. In Fig. 1c the Raman spectrum exhibits vibration bands at 145, 356, 386, 529, 566 and 619 cm^{-1}, related to α-MnOOH phase [17]. The vibrations at 566 and 619 are attributed to the stretching modes of MnO_6 octahedral sites [18]. The bands at 552 and 148 cm^{-1} are related to the presence of H^+ within the structure in the Groutite phase [17,19]. Fig. 1b and d show the SEM images of the α-MnO_2 and α-MnOOH nanorods materials, respectively. In Fig. 1b the α-MnO_2 nanorods with diameters of 50–180 nm are observed. These exhibit a tunnel structure parallel to lengthwise direction, and the length can achieve a few microns. Fig. 1d shows the SEM image of α-MnOOH. It can be observed that this material also exhibits nanorod morphology with diameters of 32–64 nm and length of a few microns.

3.2. Thermal analysis

In order to establish an appropriate heat treatment to achieve the desired spinel structure, thermal gravimetric analysis (TGA) was carried out on the synthesized precursor materials after lithium and nickel incorporations, according to the procedure explained in the Experimental section. In order to differentiate the spinels obtained, samples were named as follows: S1-LMNO spinel obtained from α-MnO_2 precursor and S2-LMNO spinel obtained from α-MnOOH precursor. Fig. 2 shows the TGA curves performed on the α-MnOOH and α-MnO_2 after lithium and nickel incorporations. As can be seen, four important regions are distinguished in the TGA curves of the two materials. The first region between 80 and 150 °C is associated with the water vaporization

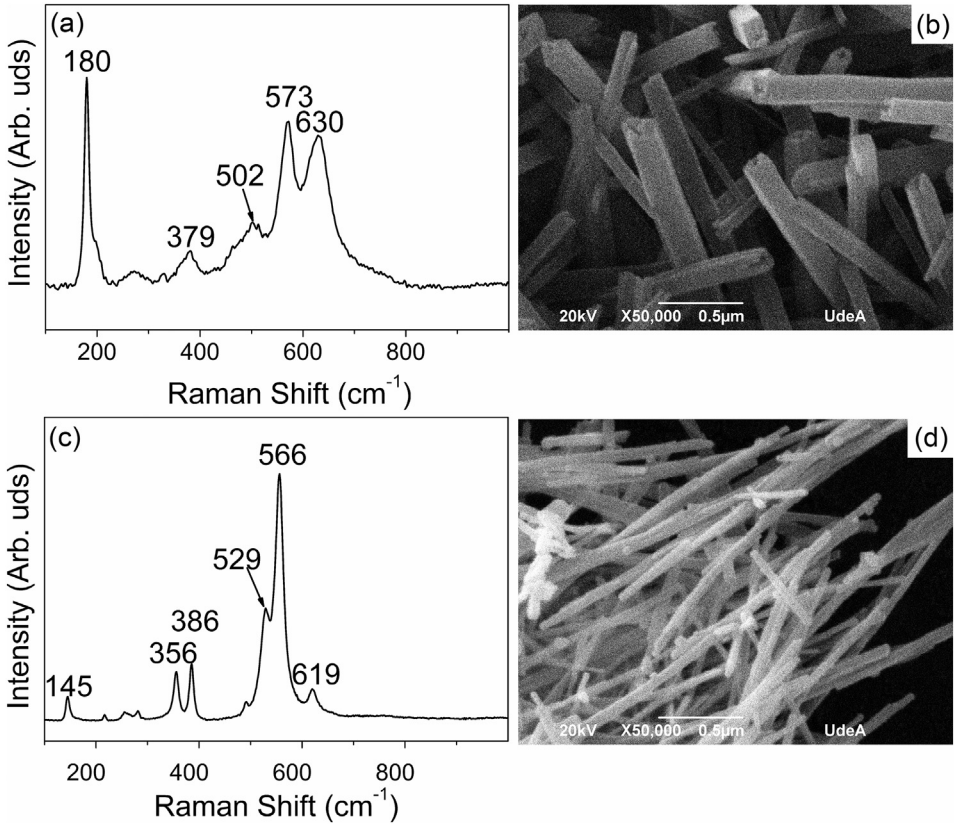

Fig. 1. Raman spectrum and SEM images of the nanorod structures of the oxide and oxyhydroxide manganese precursors synthesized by hydrothermal method. (a) and (b) α-MnO_2. (c) and (d) α-MnOOH.

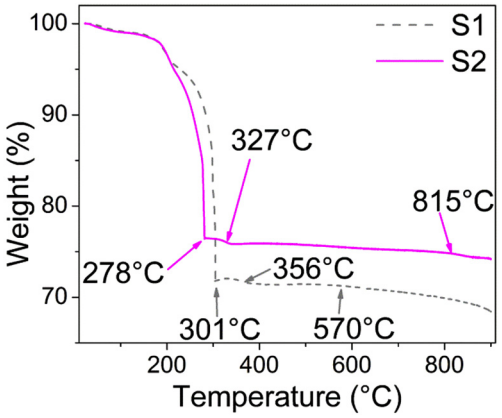

Fig. 2. TGA curves performed to the α-MNO_2 and α-MnOOH nanorods after lithium and nickel incorporations.

present in the samples. The second region, between 200 and 278 °C for α-MnOOH and between 200 and 301 °C for α-MnO_2, is associated with the decomposition of the organic part of the precursors used in the synthesis. The plateau region at intermediate temperatures between 300 and 650 °C, is where the spinel formation and lithium and nickel incorporation take place [20]. In the last region, at high temperatures > 650 °C a slight decay of the mass with the increase in temperature is observed, which is associated with the spinel decomposition and the formation of impure phases [21]. The decomposition temperature of S1 spinel obtained from α-MnO_2 nanorods precursor was lower (570 °C) than S2 spinel obtained from α-MnOOH nanorods precursor (815 °C). This behavior has also been observed in another work [22]. According to these results, more impure phases are expected in the S1 than S2 spinel, which will be corroborated later.

3.3. Spinel characterization

The morphology, phase purity and crystallographic order of the obtained spinels were characterized by TEM, Raman spectroscopy and X-ray diffraction techniques. Fig. 3 shows the TEM images and Raman spectra of $LiMn_{1.8}Ni_{0.2}O_4$ spinel nanorods, S1 and S2, obtained respectively from α-MnO_2 and α-MnOOH precursor phases. The observed diameters of the nanorods were 69.6 and 28.7 nm for spinels S1 and S2 respectively. Additionally, TEM images show tetragonal precipitates of nickel-rich spinel and nickel oxides. Chemical composition carried out by EDS (Table 1) evidenced the presence of nickel, manganese and oxygen. The nanorod structures were constituted mainly by manganese and oxygen, with little content either of nickel or, probably, lithium (not calculated by this technique). On the other hand, the precipitate phase shows a high content of nickel for S2 spinel and low content of nickel for S1 spinel. The S1 spinel nanorod showed a radial variation in density, probably due to the poor formation of the spinel structure inside the nanorods. On the other hand, the S2 spinel showed uniform density throughout its diameter. The lower diameter of S2 spinel would ease lithium insertion within the structure [23].

The Raman spectrum of S1 spinel exhibited vibration bands at 161, 401, 496 and 637 cm^{-1} associated with the cation-ordered (P4332) spinel phase [24], The shoulder band at 596 cm^{-1} is attributed to the stretching vibration mode within the MnO_6 groups of λ-MnO_2 with space groups Fd3m (disordered spinel) [25]. Raman vibrations at 401 and 496 cm^{-1} are associated to Ni—O stretching and the band at 637 cm^{-1} is assigned to Mn—O vibration [24]. The S2 spinel exhibited vibration bands located at 157, 400, 498 and 630 cm^{-1} with a shoulder band at 580 cm^{-1} or 588 due to F_{2g} vibration mode within oxygen deficient MnO_6 groups (disordered-spinel) [25,26]. The asymmetric band at 630 cm^{-1} is assigned to Mn—O stretching vibrations within MnO_6 groups. Additionally, Raman vibration at 157 or 161 cm^{-1} was

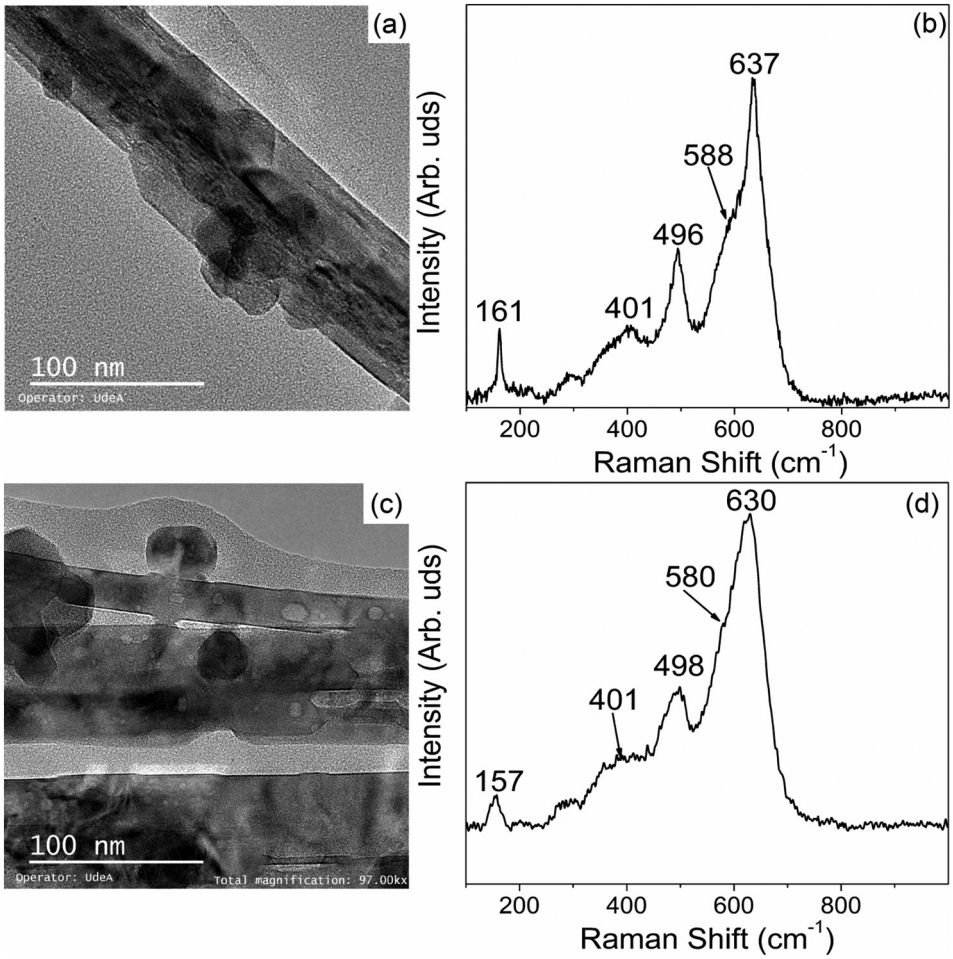

Fig. 3. TEM images and Raman spectra of $LiMn_{1.8}Ni_{0.2}O_4$ spinel nanorods. (a) and (b) spinel S1. (c) and (d) spinel S2.

Table 1
EDS analysis to determinate nanorods and precipitates chemical composition.

Element	S1-LMNO (at.%)		S2-LMNO (at.%)	
	Precipitate	Nanorods	Precipitate	Nanorods
Mn	27.1	26.5	25.4	24.1
Ni	0.8	1.1	0.94	0.58
O	71.2	68.7	73.7	75.3
K	0.93	3.7	–	–

related to separate Ni and Mn sites within the spinel structure [27]. This vibrational mode indicates that there is a phase segregation of the spinels. The Raman spectra were consistent with the chemical composition characterized by the EDS analysis, shown in Table 1. According to this, nanorods and tetragonal particle precipitates exhibit similar chemical composition. Also, the manganese/oxygen ratio content was consistent with the composition expected for a manganese spinel. Nevertheless, some impurities were found in both spinels. The S1 spinel showed potassium atomic percentages close to 4 inside the nanorods;

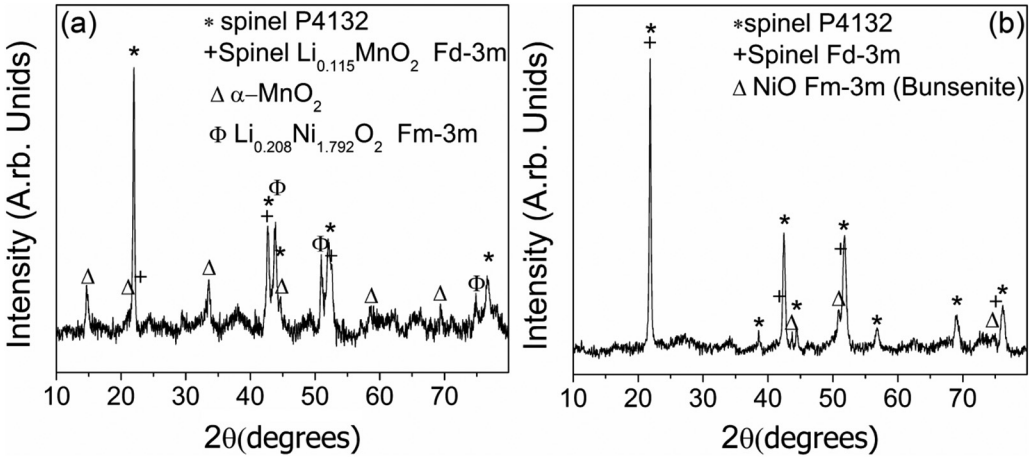

Fig. 4. Diffractograms of $LiMn_{1.8}Ni_{0.2}O_4$ spinels. (a) S1 and (b) S2.

while the S2 spinel presented some nickel oxide particles.

TEM images of the spinel nanorods were also used to calculate the interplanar spacing of the spinel crystals and to verify the crystal structure of the nanorods. GATAN Inc. software was used to measure the interplanar spacing at several radial distances. The calculated values of the (111) plane were 4.8 ± 0.5 Å and 4.8 ± 0.2 Å for the S1 and S2 spinels respectively. Considering the standard deviation of those values, it can be inferred that the same interplanar distance is obtained for both S1 and S2 spinel structures. The values of the interplanar distance between the planes were similar to the values that have been reported for manganese spinel [28,29].

Fig. 4 shows the diffractograms of S1 and S2 spinels. The goodness of fit of the refinement procedures were 0.95 and 0.88 for the S1 and S2 spinels, respectively. The pattern of the S1 sample, Fig. 4a, corresponds to nickel-manganese spinel with a cubic structure in a spatial group $P4_332$ (39%), and manganese spinel with space group $Fd\overline{3}m$ (18%). Additionally, some impurities of MnO_2 (24%) and $Li_xNi_yO_2$ (19%) were observed in the structure. The pattern of the S2 sample, Fig. 4b, corresponds to the nickel-manganese spinel phase with cubic structure in a spatial group $P4_332$ (66%) and manganese spinel with $Fd\overline{3}m$ space groups (26%) in which lithium ions occupy the 8a sites, the manganese are randomly distributed in 16d sites and oxygen ions occupy the 32e sites [30]. For the spatial group $P4_332$, the lithium ions occupy the 8c sites, the manganese ions occupy the 12d sites, the nickel occupies the 4a sites and oxygen occupies positions 8c and 24e [30]. In this sample, NiO impurity (8%) was also observed in the precipitate phase.

According to the TGA results (Fig. 2), it was found that the optimal temperature of heat treatment to promote the spinel structure formation and metals incorporation, without compromised the structure stability, was 650 °C. However, at this temperature is possible that some impurities can be formed. This is a normal situation according to the followed synthesis route. The formation of impure phases together with spinel structure is normally reported in many works [31–34]. The important issue to be considered is that the amount of impurities be as low as possible, in order to not compromises the charge density of the cathode material, this because the impurities contribute to the mass of the cathode but they do not contribute to the charge (there is not lithium intercalation in these materials).

Crystallite diameters of the spinels were estimated by Scherrer equation (Eq. (1)).

$$d = \frac{K*\lambda}{\beta \cos\theta} \quad (1)$$

where, K is the shape factor 0.9, λ is incident X-ray wavelength (0.1541874 nm) and β is the width at half maximum [26,35].

Average crystallite sizes calculated for S1 and S2 spinels were 29.0 nm and 28.9 nm respectively. The lower crystallite diameter in the LMNO-MnO_2 spinel could be related to the presence of several crystallites inside the nanorods. For the S2 spinel the crystallite size was approximately equal to the diameter of the nanorods. Therefore, it can be said that S2 nanorods were constituted mainly by mono-crystallites aggregated in axial direction. Furthermore, the d-spacing of the spinel crystals, calculated through the peak with higher intensity, exhibited values of 4.6972 Å and 4.7169 Å for S1 and S2 spinels, respectively. These results are consistent with values reported for TEM analysis performed on spinel nanorods reported in other works [36]. Additionally, some authors have related the superior interplanar spacing with the presence of a disordered spinel [37].

3.4. Electrochemical performance

Fig. 5 shows the initial galvanostatic discharge profiles and the cycling performance of the S1 and S2 spinels. The values of the specific capacities of the S1 and S2 spinels were 80 mA h g^{-1} and 125 mA h g^{-1}, respectively. The initial discharge capacities of the S1 and S2 spinel performed at a discharge rate of 0.5 C are shown and compared in Fig. 5a. Both materials show two plateaus at around 4.7 V and 4.0 V associated respectively with the Ni^{2+}/Ni^{4+} and Mn^{3+}/Mn^{4+} redox potentials vs. Li/Li^+ [38]. It is important to highlight that the S2 spinel exhibited larger charge capacity (125 mA h g^{-1}) than the S1 (80 mA h g^{-1}) and the plateau at 4.0 V of S2 spinel tended to be constant for more time. Moreover, the contribution of Ni^{2+} to the total capacity in the S2 spinel was 28% compared with 17% in the S1 spinel. This result is common for a spinel with low nickel contain [39], like the LMNO spinel here studied, which has a Ni content of 0.2. Additionally, the high charge capacity exhibited by S2 indicates that in this spinel the nickel cations are better inserted within the structure. Although, as reported in several papers, nickel decreases the spinel charge capacity for manganese spinel, (theoretical capacity of 147.6 mA h g^{-1} for LMNO compared to 148.2 mA h g^{-1} for LMO) [5,36], the $LiMn_{1.8}Ni_{0.2}O_4$ spinels obtained in this work showed higher capacity than LiMnO4 spinels reported in other works [9].

Comparing the total impurities percentage for S1 (43%) and S2 (8%) and knowing that the impurities reduce the quantity of active material with sites available to lithium intercalation, it is expected that the initial discharge capacity with respect to theoretical capacity (147.6 mA h g^{-1}) will be at the most 57% (84.1 mA h g^{-1}) for S1 and 92% (132.8 mA h g^{-1}) for S2. Those results are consistent with the initial capacity experimentally obtained for both spinels.

Furthermore, S2 spinel shows superior capacity to other spinels with nanorod morphology synthesized by other routes (120 mA h g^{-1}) [39]. Table 2 shows a comparison of the charge capacity values of manganese spinel materials with different morphologies reported in the literature, and the values in the present work. As can be seen, the S2 spinel obtained in the present work exhibits superior charge capacity than other similar materials.

The cycling performance of S1 spinel was quite different to that exhibited by S2 spinel. As can be seen in Fig. 5b, the capacity retention at several cycles of S2 spinel was always superior to that of S1 spinel. A fast decay of the discharge capacity at C/2 and C are observed for S1 spinel. Conversely, S2 spinel exhibited slow decay in discharge capacity at the same rates. After the 25th cycle the discharge test was interrupted in order to perform electrochemical impedance, cyclic voltammetry and rate capability tests. The discharge test then continued at a rate of 1 C. As can be observed in Fig. 5b, at the end of the discharge test (120th cycle) the capacity exhibited by S1 spinel was below 20 mA h g^{-1}. In contrast, S2 spinel showed a capacity close to 60 mA h g^{-1}. This result indicates that S1 spinel presents a lower calendar life than S2 spinel, probably due to superior reactivity of S1 spinel with the electrolyte [40]. The cycling stability of S2 spinel could be affected for calendar life, however comparing the spinel performance with other works on the 25th cycle, the stability is similar to other materials evaluated at high cycling rate [9,14].

It is commonly reported in literature that capacity retention decreases as C-rate increases, mainly due to the increase in internal resistance and the existence of diffusion limitation of the Li^+ ion. Fig. 6 shows the rate capability performance of the S1 and S2 spinels. As can be seen, S2 spinel exhibited high stability when C-rate was increased and was able to retain > 80% (see Fig. 6a) of the initial capacity at 5 C. This result could be related to the short diffusion length of lithium ions within S2 nanorods [41]. At C-rates higher than 5 C, the capacity decreased quickly due to restriction of the charge transfer process by the electrical conductivity of the structure [40]. However, the capacity retention evaluated at different C-rates of the S2 spinel was always higher than that exhibited by the S1 spinel. Fig. 6b shows the galvanostatic discharge profiles of S2 spinel at different C-rates. Two pseudo-plateaus are clearly differentiated between 4.8 and 4.5 V and 4.2–4.0 V, corresponding to redox pairs of Ni^{2+}/Ni^{4+} and Mn^{3+}/Mn^{4+}, respectively. It was observed that at C-rates below 2 C, the discharge potential of S2 spinel was maintained at an approximately constant potential value, indicating low variation of the internal resistance and high Li^+ ion mobility during the charge delivery in the spinel.

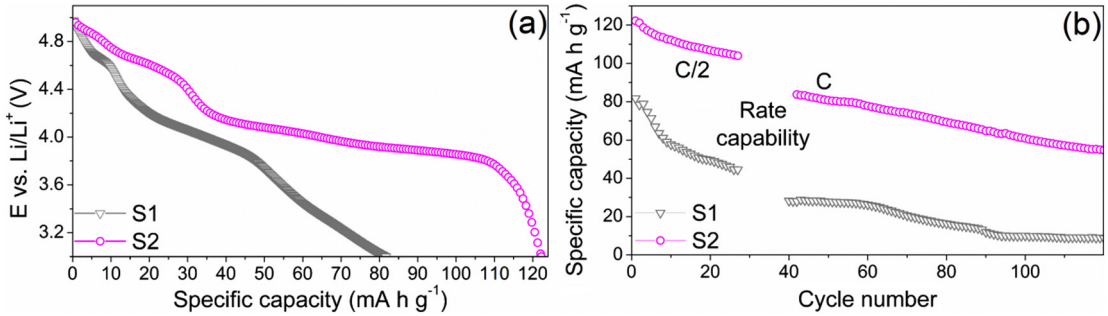

Fig. 5. (a) Initial galvanostatic discharge profiles of S1 and S2 spinels performed at 0.5 C. (b) Cycling performance at C/2 and C rates.

Table 2
Comparative capacity for spinels obtained in previous works.

Spinel morphology	Discharge rate	Capacity (mA h g^{-1})	Reference
$LiMn_{1.8}Ni_{0.2}O_4$-spherical	0.2 C	110	[39]
$LiMn_2O_4$-nanorods	1 C	120	[9]
$LiMn_{1.5}Ni_{0.5}O_4$-nanorods	1 C	71	[37]
$LiMn_{1.5}Ni_{0.5}O_4$-orthorombic	1 C	122	[37]
S2-nanorods	1 C	125	This work

To understand the C-rate discharge response, the kinetic parameters were evaluated by cyclic voltammetry and electrochemical impedance spectroscopy. Cyclic voltammetry is a powerful technique for evaluating lithium diffusion within the structure of the active material. This is because during the CV test there is a relationship between the current peak and the scan rate of the CV curves caused by the diffusion process [42]. The apparent diffusion coefficient can be estimated using the CV curves. Fig. 7a shows the CV curves of the S1 and S2 spinels performed at a scan rate of 0.2 mV s^{-1}. In the low voltage range, S1 spinel exhibits two anodic current peaks at 4.1 and 4.2 V and two cathodic current peaks at 3.9 and 4.1 V, related to Mn^{3+}/Mn^{4+} pair redox. Similarly, for S2 spinel the anodic and cathodic peaks in the low voltage range related to Mn^{3+}/Mn^{4+} pair redox are more clearly identified at 4.2 and 4.3 V vs. Li/Li^+ and at 4.0 and 3.8 V vs. Li/Li^+, respectively. The presence of two pair redox peaks in the low voltage range indicates that these spinels also contain disorder phase [37]. In the high voltage range, S1 spinel exhibits one anodic current peak and one cathodic current peak at 4.8 and 4.7 V respectively, related to Ni^{2+}/Ni^{4+} pair redox. Meanwhile, S2 spinel exhibits the Ni^{2+}/Ni^{4+} pair redox at 4.8 and 4.6 V. The current peaks exhibited by S2 spinel are always higher than those exhibited by S1 spinel. This result is associated with the larger number of lithium intercalation sites within the S2 spinel structure. A linear relationship was found between the first anodic current peak (I_p) in the low voltage range and the square root of the scan rate for both spinel samples, shown in Fig. 7b. This could be related to the diffusion process of Li^+ ion [29]. The apparent diffusion coefficient of Li^+ can be estimated for comparison purpose between S1 and S2 spinels using Eq. (2) [29,43,44].

$$I_p = 4.64 \times 10^6 n^{3/2} A * T^{-1/2} D^{1/2} C_{Li} \nu^{1/2} \quad (2)$$

where I_p is the peak current (A), n is the electrons transfer number during the structure oxidation (1); A is the surface area calculated from TEM images as 2.06E + 05 $cm^2\,g^{-1}$ and 3.57E + 05 $cm^2\,g^{-1}$ for S1 and S2 spinels respectively; C_{Li} is the concentration of lithium within the cathode electrode (0.0238 mol cm^{-3}); T is the temperature (293 K); ν is the scan rate (V s^{-1}); and D is the apparent diffusivity ($cm^2\,s^{-1}$) [29,43,44]. The apparent diffusivity coefficients calculated for S2 and S1 spinels were 8.99E − 9 and 2.82E − 9 $cm^2\,s^{-1}$ respectively [42]. The apparent diffusivity of S2 spinel is higher than that of S1 spinel. Therefore, lower lithium intercalation time and higher charge capacity at high charge rates are expected for S2 spinel than for S1 spinel.

Electrochemical impedance spectroscopy (EIS) performed at 50% of charge on S1 and S2 spinels are shown as Nyquist diagrams in Fig. 8a. Two capacitive loops and linear behavior are observed in the EIS diagrams for both spinels. The first capacitive loop at high frequencies (0.1–1 kHz) is associated with the SEI film capacitance in parallel with SEI resistance. The second capacitive loop, at intermediate frequencies (< 1 Hz), is associated with the charge transfer resistance in parallel with the double layer capacitance of the active material. The linear region at low frequencies is due to the diffusion process of lithium ions within the spinel crystallites.

A fit of the experimental EIS results (lines in the Nyquist plots) was performed using the equivalent electrical circuit shown in the inset of Fig. 8. Electrical parameter values of the spinels were calculated using Gamry software and are shown in Table 3. The effective capacitance of the double layer was calculated using Eq. (3). The effective SEI capacitance was calculated using Eq. (4). For S2 spinel, the double layer capacitance was higher than the respective value for S1 spinel. This is associated with the higher surface area exhibited for the S2 spinel. In this structure, the SEI resistance increases with the cycle number as the electrolyte degrades the active material. The SEI thickness decreased as it was dissolved in the electrolyte. Additionally, the charge transfer

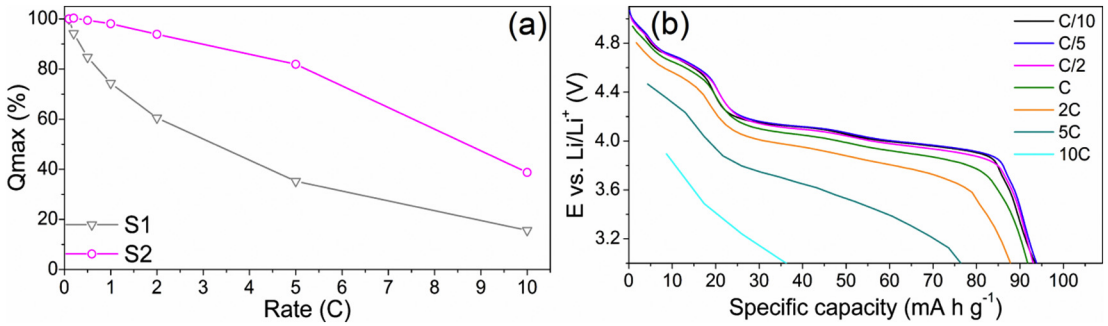

Fig. 6. (a) Rate capability of spinels S1 and S2 at room temperature after 25th cycle, with a charge rate of 0.5 C. (b) Galvanostatic discharge profiles of S2 spinel performed at different C-rates.

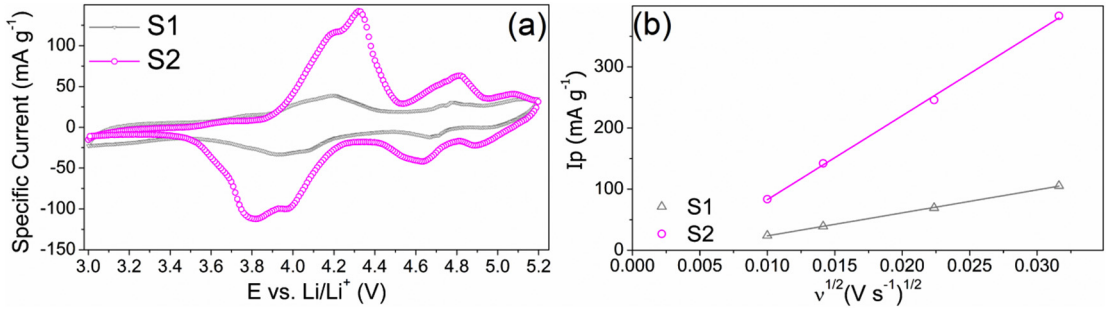

Fig. 7. (a) Cyclic voltammograms of S1 and S2 spinels performed at a scan rate of 0.2 mV s^{-1}. (b) Variation of the current density of the first anodic current peak (I_p) in the low voltage range with the square root of the scan rate during the CV test.

resistance in the active material increases with cycle number by a factor of 3. The changes in the electrical parameters of the S2 spinel with the cycle number induces changes in the time constants of the electrochemical processes that occur in the SEI and the active material. This produces a coupling between the capacitive loops at high and intermediate frequencies in the impedance diagrams obtained at high cycle numbers.

The diffusivity was calculated using Eq. (5), where the "t" is the intercalation time (parameter B) and $\phi_{1/2}$ is half of intercalation distance [45]. The $\phi_{1/2}$ values were calculated using the TEM image, taking values of 2.24E−06 cm and 1.30E−06 cm for S1 and S2 spinels, respectively. The S2 spinel shows a lower diffusion time than the S1 spinel. This is associated with the smaller nanorod diameter exhibited by S2 spinel, which reduces the diffusion distance for Li^+ ions transport. Also, diffusion coefficients were 9.85E−14 and 8.52E−13 $cm^2 s^{-1}$ for spinels S1 and S2, respectively. These values are in the same range of diffusivity values reported in the literature (10^{-10}–10^{-16} $cm^2 s^{-1}$) [30]. The S2 spinel nanorods present a higher diffusion coefficient than that exhibited for S1 spinel, which may be because S2 spinel was mainly constituted of mono-crystallites. These results are coherent with the preservation of a larger charge capacity at high charge rates observed for S2 spinel in comparison to S1.

$$Ceff. = \left[Q\left(\frac{1}{R_s} + \frac{1}{R_p}\right)^{(\alpha-1)} \right]^{1/\alpha} \quad (3)$$

$$Ceff.film = Q^{\frac{1}{\alpha}} R_{SEI}^{(1-\alpha)/\alpha} \quad (4)$$

where, "Rs" is the series resistance "Rp" is parallel resistance, R_{SEI} is the SEI resistance "α" is the exponential factor and "Q" is the pseudo-capacitance [45].

$$D = (\varphi_{1/2} * t)^2 \quad (5)$$

4. Conclusions

In the present work, an alternative route showing an ecological method to synthesize α-MnOOH as intermediate phase was developed. These results in increased load capacity and velocity compared to spinel obtained by intermediate α-MnO_2.

The use of intermediate phase to synthesize the spinel materials guaranteed the morphology and particle size control, given that the final products conserved the initial structure and morphology.

The α-MnOOH starting phase allowed spinels with higher quality than the α-MnO_2 intermediate to be obtained, since the residual elements in α-MnOOH synthesis were burned during the heat treatment. Additionally, the α-MnOOH nanorods were constituted by mono-crystallites and the diameter of the nanorods was smaller and more homogeneous than the α-MnO_2 diameter, which makes lithium intercalation and nickel insertion processes easier during the solid state synthesis stage.

The α-MnOOH synthesis route is a promising option to obtain cathode materials for high rate batteries that can be used for electric cars, given that this material would be discharged in a time of 12 min

Table 3
Electrical parameters of S1 and S2 spinels obtained by fitting of the EIS experimental results at 50% of charge using the electrical equivalent circuit (inset of Fig. 8).

Parameters	S1 spinel 25th cycle	S2 spinel 25th cycle	S2 spinel 120th
Rs (ohm g)	7.42E−02	5.27E−02	10.66E−2
Ceff. SEI (μF g^{-1})	11.15E+02	5.49E+02	8.28E+02
δ SEI (cm)	5.43E−12	6.38E−12	4.23E−12
R SEI (ohm g)	5.12E−01	6.23E−01	14.67E−01
T SEI (s)	5.71E−04	3.42E−04	12.15E−04
Ceff.dl (μF g^{-1})	6.31E+06	21.2E+06	0.05+06
Rct (ohm g)	2.85E−02	15.8E−02	44.94E−02
T_{Rct} (s)	1.80E−01	33.6E−1	0.22E−01
Yo_{16} (S $s^{\wedge 1/2}$ g)	9.85E−05	2.85E−06	2.54E−04
B ($s^{\wedge 1/2}$)	7.12	1.40	11.85
Diffusivity ($cm^2 s^{-1}$)	9.85E−14	8.52E−13	1.19E−14
Goodness of fit	2.14E−04	1.14E−04	7.03E−04

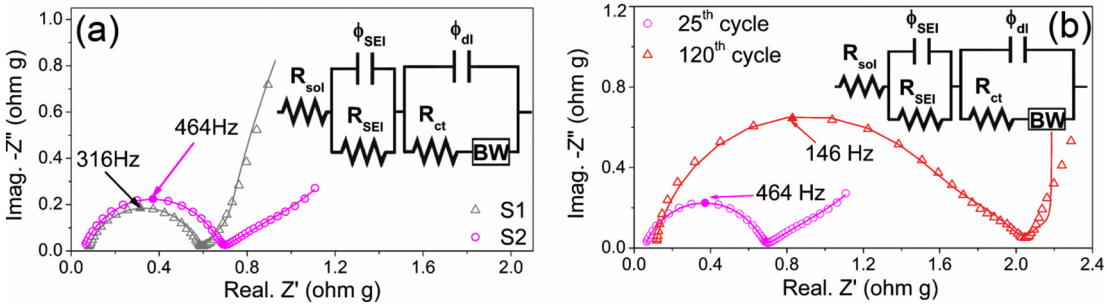

Fig. 8. (a) Electrochemical impedance of spinels S1 and S2 performed at 50% of charge. (b) Comparative electrochemical impedance performed of S2 spinel after 25th and 120th cycles. Experimental values (dots), fitted values (lines).

while keeping > 80% of initial charge capacity, with an energy density of 488 mW h g^{-1}.

Acknowledgments

The authors thank the “Departamento Administrativo de Ciencia, Tecnología e Innovación - COLCIENCIAS” for their financial support through the project 1115-745-58653. Author F. A. Vásquez wishes to thank COLCIENCIAS for his doctoral scholarship grant. Authors also acknowledge the Instituto de Investigaciones Fisicoquímicas Teóricas y Aplicadas (INIFTA) of Argentine for their technical support.

References

[1] N.S. Lewis, Powering the planet, Mater. Res. Soc. Spring Meet. 32 (10) (2007) 808–820.
[2] IEA, International Energy Agency Key World Energy Statistics 2011, [Online]. Available, 2011. http://www.iea.org/publications/freepublications/publication/key_world_energy_stats-1.pdf, .
[3] K. Kieckhäfer, K. Wachter, T.S. Spengler, Analyzing manufacturers â€™ impact on green products â€™ market diffusion-the case of electric vehicles, J. Clean. Prod. 162 (2017) 11–25.
[4] J.D. Adler, P.B. Mirchandani, G. Xue, M. Xia, The electric vehicle shortest-walk problem with battery exchanges, Springer Sci. 17 (2014) 1572–9427.
[5] N. Nitta, F. Wu, J.T. Lee, G. Yushin, Li-ion battery materials: present and future, Mater. Today 18 (5) (2015) 252–264.
[6] R. Chen, T. Zhao, X. Zhang, L. Li, F. Wu, Advanced cathode materials for lithium-ion batteries using nanoarchitectonics, Nanoscale Horiz. 1 (2016) 423–444.
[7] A. van der Ven, J. Bhattacharya, A.A. Belak, Understanding Li diffusion in Li-intercalation compounds, Acc. Chem. Res. 46 (5) (2011) 1216–1225.
[8] E.S. Pampal, E. Stojanovska, B. Simon, A. Kilic, A review of nanofibrous structures in lithium ion batteries, J. Power Sources 300 (2015) 199–215.
[9] Z. Bai, N. Fan, Z. Ju, C. Sun, Y. Qian, $LiMn_2O_4$ nanorods synthesized by MnOOH template for lithium-ion batteries with good performance, Mater. Lett. 76 (2012) 124–126.
[10] W. Xiao, W. Liu, X. Mao, H. Zhu, D. Wang, Chemical mixing in molten-salt for preparation of high-performance spinel lithium manganese oxides: duplication of morphology from nanostructured MnO_2 precursors to targeting materials, Electrochim. Acta 88 (2013) 756–765.
[11] J. Shu, et al., Comparison of electronic property and structural stability of $LiMn_2O_4$ and $LiNi_{0.5}Mn_{1.5}O_4$ as cathode materials for lithium-ion batteries, Comput. Mater. Sci. 50 (2010) 776–779.
[12] L. He, S. Zhang, X. Wei, Z. Du, G. Liu, Y. Xing, Synthesis and electrochemical performance of spinel-type $LiMn_2O_4$ using γ-MnOOH rods as self-template for lithium ion battery, J. Power Sources 220 (2012) 228–235.
[13] J. Luo, et al., Synthesis of single-crystal tetragonal MnO_2 nanotubes, J. Phys. Chem. Lett. 112 (2008) 12594–12598.
[14] D. Zhan, F. Yang, Q. Zhang, X. Hu, T. Peng, Effect of solid-state reaction temperature on electrochemical performance of $LiMn_2O_4$ submicro-rods as cathode material for Li-ion battery by using γ-MnOOH submicro-rods as self-template, Electrochim. Acta 129 (2014) 364–372.
[15] K. Abdelazez, M. Ahmed, Exploitation of $KMnO_4$ material as precursors for the fabrication of manganese oxide nanomaterials, J. Taibah Univ. Sci. 10 (2016) 412–429.
[16] T. Gao, H. Fjellvåg, P. Norby, A comparison study on Raman scattering properties of alfa and beta-MnO_2, Anal. Chim. Acta 648 (2009) 235–239.
[17] S. Cheng, et al., Phase evolution of an alpha MnO_2-based electrode for pseudocapacitors probed by in operando Raman spectroscopy, Nano Energy 9 (2014) 161–167.
[18] C.M. Julien, M. Massot, C. Poinsignon, Lattice vibrations of manganese oxides. Part I. Periodic structures, Spectrochim. Acta 60 (2004) 689–700.
[19] B. Marie-Claude, et al., Electrochromic reactions in manganese oxides I. Raman analysis, J. Electrochem. Soc. 140 (1993) 3065–3070.
[20] H. Liang, X. Zhao, Z. Yu, M. Cao, H. Liu, Effect of ultrasonic irradiation on structure and electrochemical properties of $LiMn_2O_4$ thin films cathode material for Li-ion micro-batteries, Solid State Ionics 192 (1) (2011) 339–342.
[21] A. Choi, et al., Microwave-assisted hydrothermal synthesis of electrochemically active nano-sized Li_2MnO_3 dispersed on carbon nanotube network for lithium ion batteries, J. Alloys Compd. 591 (2014) 356–361.
[22] Xin Yi, et al., Elevated temperature cyclic performance of $LiAl_xMn_{2-x}O_4$ microspheres synthesized via co-precipitation route, J. Alloys Compd. 604 (2014) 50–56.
[23] T.V.S.L. Satyavani, B. Ramya Kiran, V. Rajesh Kumar, A. Srinivas Kumar, S.V. Naidu, Effect of particle size on dc conductivity, activation energy and diffusion coefficient of lithium iron phosphate in Li-ion cells, Eng. Sci. Technol. Int. J. 19 (2016) 40–44.
[24] X. Zhang, F. Cheng, J. Yang, J. Chen, $LiNi_{0.5}Mn_{1.5}O_4$ porous nanorods as high-rate and long-life cathodes for Li-ion batteries, Nano Lett. 13 (2013) 2822–2825.
[25] C.M. Julien, M. Massot, Lattice vibrations of materials for lithium rechargeable batteries. I. Lithium manganese oxide spinel, Mater. Sci. Eng. B B97 (2003) 217–230.
[26] D. Liu, et al., Spinel materials for high-voltage cathodes in Li-ion batteries, RSC Adv. 4 (2014) 154–167.
[27] J. Song, D.W. Shin, Y. Lu, C.D. Amos, A. Manthiram, J.B. Goodenough, Role of oxygen vacancies on the performance of $Li[Ni_{0.5-x}Mn_{1.5+x}]O_4$ (x = 0, 0.05, and 0.08) spinel cathodes for lithium-ion batteries, Chem. Mater. 24 (2012) 3101–3109.
[28] J.S. Kim, K. Kim, W. Cho, W.H. Shin, R. Kanno, J.W. Choi, A truncated manganese spinel cathode for excellent power and lifetime in lithium-ion batteries, Nano Lett. 12 (2012) 6358–6365.
[29] H. Liu, et al., Morphological evolution of high-voltage spinel $LiNi_{0.5}Mn_{1.5}O_4$ cathode materials for lithium-ion batteries: the critical effects of surface orientations and particle size, ACS Appl. Mater. Interfaces 8 (2016) 4661–4675.
[30] B. Xu, D. Qian, Z. Wang, Y.S. Meng, Recent progress in cathode materials research for advanced lithium ion batteries, Mater. Sci. Eng. 73 (2012) 51–65.
[31] T.-F. Yi, J. Mei, Y.-R. Zhu, Key strategies for enhancing the cycling stability and rate capacity of $LiNi_{0.5}Mn_{1.5}O_4$ as high-voltage cathode materials for high power lithium-ion batteries, J. Power Sources 316 (2016) 85–105.
[32] J.-W. Lee, J.-I. Kim, K.C. Roh, Lithium manganese oxide with excellent electrochemical performance prepared from chemical manganese dioxide for lithium ion batteries, Solid State Sci. 14 (9) (2012) 1251–1255.
[33] Y. Qian, Y. Deng, Z. Shi, Y. Zhou, Q. Zhuang, Guohua Chen, Sub-micrometer-sized $LiMn_{1.5}Ni_{0.5}O_4$ spheres as high rate cathode materials for long-life lithium ion batteries, Electrochem. Commun. 27 (2013) 92–95.
[34] I.M. Hung, Y.C. Yang, H.J. Su, J. Zhang, Influences of the surfactant on the performance of nano-$LiMn_2O_4$ cathode material for lithium-ion battery, Ceram. Int. 41 (2015) S779–S786.
[35] A. Monshi, M.R. Foroughi, M.R. Monshi, Modified Scherrer equation to estimate more accurately nano-crystallite size using XRD, World J. Nano Sci. Eng. 2 (2012) 154–160.
[36] X. Zhang, H. Zheng, V. Battaglia, R.L. Axelbaum, Flame synthesis of 5 v spinel-$LiNi_{0.5}Mn_{1.5}O_4$ cathode-materials for lithium-ion rechargeable-batteries, Proc. Combust. Inst. 33 (2011) 1867–1874.
[37] S. Hong, S. Mho, I. Yeo, Y. Kang, D. Kim, Structural and electrochemical characteristics of morphology-controlled $Li[Ni_{0.5}Mn_{1.5}]O_4$ cathodes, Electrochim. Acta 156 (2015) 29–37.
[38] Z.-G. Gao, et al., High performance 5 V $LiNi_{0.5}Mn_{1.5}O_4$ spinel cathode materials synthesized by an improved solid-state method, Electrochim. Acta 654 (2016) 257–263.
[39] M.A. Kebede, N. Kunjuzwa, C.J. Jafta, M.K. Mathe, K.I. Ozoemena, Solution-combustion synthesized nickel-substituted spinel cathode materials ($LiNi_xMn_{2-x}O_4$; $0 \le x \le 0.2$) for lithium ion battery: enhancing energy storage, capacity retention, and lithium ion transport, Electrochim. Acta 128 (2014) 172–177.
[40] C. Julien, A. Mauger, A. Vijh, K. Zaghib, Lithium Batteries Science and Technology, New York (2016).
[41] Y. Chen, K. Xie, Y. Pan, C. Zheng, Nano-sized $LiMn_2O_4$ spinel cathode materials exhibiting high rate discharge capability for lithium-ion batteries, J. Power Sources 196 (2011) 6493–6497.
[42] R. Greff, R. Peat, L.M. Peter, J. Robinson, Instrumental Methods in Electrochemistry, Woodhead Publishing Limited, Philadelphia, 2011.
[43] S.-R. Li, et al., Facile synthesis of micrometer $Li_{1.05}Mn_{1.95}O_4$ and its low temperature performance for high power lithium ion batteries, Electrochim. Acta 81 (2012) 191–196.
[44] T. Yang, N. Zhang, Y. Lang, K. Sun, Enhanced rate performance of carbon-coated $LiNi_{0.5}Mn_{1.5}O_4$ cathode material for lithium ion batteries, Electrochim. Acta 56 (2011) 4058–4064.
[45] B. Hirschorn, M.E. Orazem, B. Tribollet, V. Vivier, I. Frateur, M. Musiani, Electrochimica acta determination of effective capacitance and film thickness from constant-phase-element parameters, Electrochim. Acta J. 55 (2010) 6218–6227.